# Experimental study of an off-axis three mirror anastigmatic system with wavefront coding technology

Feng Yan* and Xiaoping Tao

Key Laboratory of Optical System Advanced Manufacturing Technology, Changchun Institute
of Optics, Fine Mechanics and Physics, Chinese Academy of Science, Changchun 130033, China

*Corresponding author: yanfeng@ciomp.ac.cn

Wavefront coding (WFC) is a kind of computational imaging technique that controls defocus and defocus related aberrations of optical systems by introducing a specially designed phase distribution to the pupil function. This technology has been applied in many imaging systems to improve performance and/or reduce cost. The application of WFC technology in an off-axis three mirror anastigmatic (TMA) system has been proposed, and the design and optimization of optics, the restoration of degraded images, and the manufacturing of wavefront coded elements have been researched in our previous work. In this paper, we describe the alignment, the imaging experiment, and the image restoration of the off-axis TMA system with WFC technology. The ideal wavefront map is set to be the system error of the interferometer to simplify the assembly, and the coefficients of certain Zernike polynomials are monitored to verify the result in the alignment process. A pinhole of 20 $\mu$m diameter and the third plate of WT1005-62 resolution patterns are selected as the targets in the imaging experiment. The comparison of the tail lengths of point spread functions is represented to show the invariance of the image quality in the extended depth of focus. The structure similarity is applied to estimate the relationship among the captured images with varying defocus. We conclude that the experiment results agree with the earlier theoretical analysis.   © 2012 Optical Society of America

*OCIS codes:*   220.1140, 100.3020, 110.1758.

## 1. Introduction

The application of wavefront coding (WFC) technology can help optical digital imaging systems control defocus and defocus related aberrations such as astigmatism, Petzval curvature, and temperature-related and alignment-related defocus [1,2]. It has been applied in many fields because of its particular character [3]. Dowski *et al.* [4] illustrated an athermalized, refractive, silicon/germanium IR imaging system with WFC technology subjected to an ambient temperature range of −20 °C to +70 °C. Kubala *et al.* [5] studied the application of WFC technology on an aberration and error invariant space telescope system with a segmented primary mirror with a large aperture. Porras *et al.* [6] proposed the application of WFC technology in astronomical instruments, to correct chromatic aberration and field curvature automatically. Mezouari and Harvy [7] described the optimization of WFC technology on a thermal imaging system of fast optics and wide fields of view, to reduce weight, size, and cost while maintaining acceptable imaging performance. Chi and George [8] studied a smart camera that combines the blurring logarithmic asphere lens and maximum entropy processing to extend the depth of field and provide near diffraction-limited performance. Narayanswamy *et al.* [9] have applied WFC technology on iris recognition imaging to increase the depth of field without sacrificing signal-to-noise ratio (SNR) or resolution of the system. Cirino and Neto

[10] developed the design of inexpensive lenses for passive infrared motion sensors with WFC technology. Tremblay *et al.* [11] applied WFC technology on thin annular folded imaging systems to relax alignment and fabrication tolerances. Mouroulis [12] designed low-power microscope objectives with WFC technology, to extend depth of field while preserving resolution up to half the maximum diffraction-limited spatial frequency. Lee *et al.* [13] proposed a resolution enhancement method for mobile compact imaging systems with small $f$-numbers based on wavefront coding and super-resolution image processing. The WFC technology has also been applied in applications including optical character recognition, vision/label reading, barcode scanning, and biometric imaging. such as fingerprint recognition.

In our previous work, the WFC technology was applied on a typical Cook's three mirror anastigmatic (TMA) system (invented by Wetherell and Womble of ITEK Corp. [14]) to extend its depth of focus (DOF). The initial optical design with WFC technology was established based on a transition model, and the residual error and DOF extending factor were analyzed [15]. Optimization based on modulation transfer function (MTF) invariance was proposed, in which the genetic algorithm tool was introduced into an optical program to accelerate the optimizing process [16]. Image restoration based on regularization was studied and tested [17]. The wavefront coding element was fabricated, which was tested by nonnull interferometry based on digital reference and partial compensation [18]. The paper is organized as follows: Sections 1 and 2 briefly introduce WFC technology and some results of our previous research. Section 3 introduces autocollimated alignment with digital reference. Section 4 presents the imaging experiment of star point and a WT1005-62 resolution pattern (the WT1005-62 resolution pattern is widely used as a target for optical system testing in China; it is like the U. S. Air Force resolution target). Section 5 describes the analysis and comparison of captured and restored images. Conclusions are in the last section.

## 2. Brief WFC Introduction and System Overview

WFC technology is an innovative system-level technology that can control defocus related aberrations. The image quality of a wavefront coded system will remain nearly the same in spite of a different defocus over a much larger range than the original DOF when a special phase distribution is appended to the normal pupil function of the system through phase masking, surface modulation, or other methods. Although the image quality is degraded, it can be restored well by the proper algorithm because the introduced phase distribution is known and the degradation mechanism is clear in advance. The essential characteristic of WFC technology is a trade-off between the degradation of image quality and extension of the DOF [15,16].

The introduced phase distribution can be cubic, spherical, logarithmic, sinusoidal, petal, free form, or another form, among which the most widely used, to our knowledge, is the cubic form, shown in Eq. (1), which is very different from the pupil function of the usual optical system:

$$P_{\text{usual}} = \begin{cases} 1 & \text{for } |x^2 + y^2| \le 1 \\ 0 & \text{otherwise} \end{cases} \to P_{\text{WFC}}$$

$$= \begin{cases} \frac{1}{\sqrt{2}} \exp(j\alpha(x^3 + y^3)) & \text{for } |x^2 + y^2| \le 1 \\ 0 & \text{otherwise} \end{cases}, \quad (1)$$

where $P_{\text{usual}}$ is the ideal pupil function of the usual system and $P_{\text{WFC}}$ is that of the wavefront coded system, $x, y$ is the normalized coordinate, and $\alpha$ is the factor that determines the extent of the cubic term.

Equation (2) presents the optical transfer function (OTF) about defocus of the wavefront coded system with cubic pupil function in one dimension. Note that the defocus term is excluded in Eq. (2), which means that the MTF becomes insensitive to defocus. The MTF [the real part of Eq. (2)] becomes inversely proportional to $\alpha$, and the MTF value becomes much lower than usual, especially within the range of high spatial frequency. One can easily deduce that the PSF of the wavefront coded system with a cubic phase is triangular in appearance and will be larger than the usual PSF:

$$H(u, W_{020}) \approx \left(\frac{\pi}{12\alpha u}\right)^{1/2} \exp\left(j\frac{\alpha u^3}{4}\right) \exp\left(-j\frac{k W_{020}^2 u}{3\alpha}\right),$$
$$u \ne 0. \quad (2)$$

The sketch of the system under research and its main parameters are shown in Fig. 1. The system has a focal length of 2 m and the Nyquist spatial frequency of 57.2l p/mm for an 8.75 $\mu$m × 8.75 $\mu$m CCD pixel. The secondary mirror is selected to be the wavefront coded element. Its surface figure is shown in Eq. (3):

$$z(x,y) = \frac{c(x^2 + y^2)}{1 + \sqrt{1 - (1+k)c^2(x^2 + y^2)}} + \beta(x_n^3 + y_n^3),$$
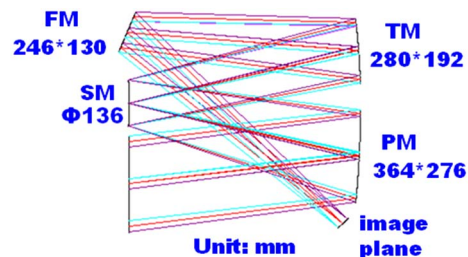$$(3)$$



Fig. 1. (Color online) Sketch and main parameters of the off-axis TMA system being researched, where PM is the primary mirror (ellipse), SM is the secondary mirror (WFC element), TM is the tertiary mirror (ellipse), and FM is the folded mirror (plane).

where $x$, $y$ are the actual coordinates, $x_n$, $y_n$ are normalized coordinates that are normalized by the radius of the mirror, and $\beta$ is the coefficient of cubic terms. Note that the surface of the secondary mirror is a kind of free-form surface, which is not rotationally symmetric. The surface figure is manufactured with both numerical control polishing and necessary handworking, and it is tested with non-null testing based on digital reference and partial compensation, which will be described in detail in a future publication.

Note that a cubic term is added to the original rotationally symmetric surface to introduce a special cubic phase distribution to the pupil function. The MTF curves of the system in the extended DOF are shown in Fig. 2, which demonstrates that the MTF values keep nearly invariant in spite of varying defocus. It has been also proven that the MTF curves in any field of view present the same behavior, and we therefore omitted figures of these curves for brevity.

## 3. Alignment

Three steps are necessary for aligning the system as shown in Fig. 3. The first step is to fix the primary mirror on a six-dimensional (6D) mount and set the position of the primary mirror as fiducial as usual. As noted earlier the system under research is Cook's TMA system, and it is designed so that the vertices of the parent mirrors of the primary mirror and the tertiary mirror coincide with each other and all three mirrors share the same optical axis, shown in Fig. 3. To take advantage of the optical design, the tertiary mirror is assembled in the second step, instead of the secondary mirror. The attitude of the tertiary mirror can be adjusted by another 6D mount, and the laser tracker is applied in the adjustment. It is very difficult to make any benchmark for alignment on both the primary mirror and the tertiary mirror, and so the two mirrors have to be assembled according to the mechanical fiducial of their junction plates to the 6D mounts. The two mirrors are fixed to their junction plates very accurately so that the angular position of the mirrors can be indicated by the junction plates. Two small mirrors are attached to two selected surfaces of each junction plate in parallel, which can be applied as the benchmark. One mirror is for elevation testing and the other mirror is for roll testing. Because the positional relationship between the primary and tertiary mirrors is clear because of the optical design, the tertiary mirror can be aligned according to the positional testing information. Two theodolites are applied in the alignment: one is to monitor the elevations of the primary mirror and the tertiary mirror, and the other is to monitor their roll with the help of another reference plane mirror. When the position and the normal of the vertex of the parent mirror of the tertiary mirror coincide with those of the primary mirror, the tertiary mirror is adjusted to the right position. The last step is to adjust the secondary mirror with the common self-collimating alignment technology. The plane mirror is located in front of the primary mirror, and the interferometer with a spherical standard lens is located where its focus coincides with the nominal image point. The secondary mirror is fixed on a 6D mount, and the plane mirror and the interferometer are fixed on two four dimensional (4D) mounts. Note that a minor adjustment of the tertiary mirror is also needed while assembling the secondary mirror, to compensate for residual errors of curvature, surface figure, etc. Only one field of view is concentrated on for simplicity, which reduces the difficulty in the alignment of the secondary mirror.

Note that the alignment of a wavefront coded system is a little different from that of an ordinary optical system: the aligning target of normal systems is to minimize the residual wavefront error, whereas the target of a wavefront coded system is to obtain a special cubic wavefront map as shown in Fig. 4(a). For convenience, the ideal wavefront map is operated as the system error file of an interferometer so that it can be subtracted automatically from the measured wavefront in each testing. Thus, the residual wavefront error between the measured wavefront and the expected wavefront map is used as the calibrating criterion. When the residual wavefront error reaches minimum, the special cubic wavefront is obtained, as shown in Fig. 4(b).

Notice that the measured wavefront map needs additional verification for assurance. The ideal cubic phase term can be expressed by the linear combination of six Zernike polynomials, as shown in Eq. (4):

$$x^3 + y^3 = \frac{1}{2}(Z_2 + Z_3) + \frac{1}{4}(Z_7 + Z_8 + Z_{10} - Z_{11}), \quad (4)$$

where $Z_2 = x$, $Z_3 = y$, $Z_7 = 3x^3 + 3xy^2 - 2x$, $Z_8 = 3y^3 + 3yx^2 - 2y$, $Z_{10} = x^3 - 3xy^2$, and $Z_{11} = -y^3 + 3x^2y$.

Clearly, the proportional relationship among the coefficients of the last four Zernike polynomials should be $1:1:1:-1$ for the ideal cubic phase term, whereas the $Z_2$ and the $Z_3$ terms are additive linear terms and can be removed. Hence, the alignment can be verified by checking the coefficients of the last four Zernike polynomials. The coefficients of Zernike
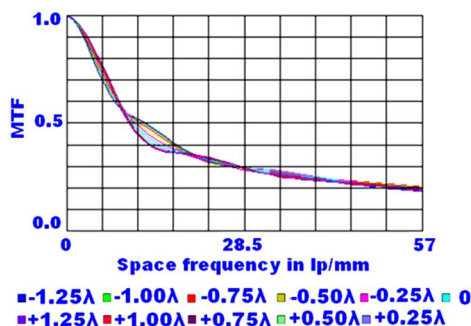
Fig. 2. (Color online) MTF curves of the optimized wavefront coding system with defocus varying from $-1.25\lambda$ to $1.25\lambda$ with increments of $0.25\lambda$ defocus.
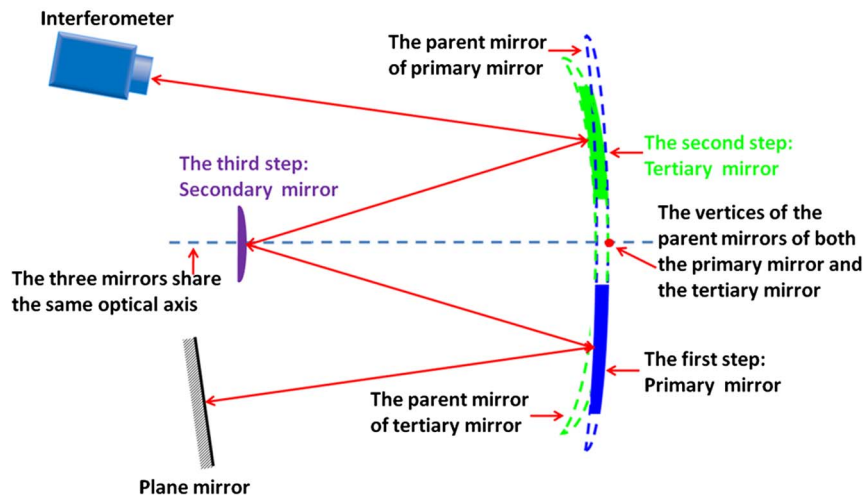
Fig. 3. (Color online) Graphical introduction of the alignment of the wavefront coding system.

polynomials of the measured wavefront as shown in Fig. 4(b) are given in Table 1.

Notice that the proportional relationship of the last four coefficients of Zernike polynomials is quite close to $1:1:1:-1$. The proportional relationship among them is not exactly $1:1:1:-1$ because of other residual errors in the system, such as the figure error of the mirrors and residual misalignment. Nevertheless, the effect of the residual error is very small and can be ignored.

## 4. Imaging Experiment

After alignment, we performed an imaging experiment. The experiment setup is shown in Fig. 5. The focal length of the collimator is 4 m; thus the magnifying ratio of the system is 2. The folded mirror of the optical system is taken off for simplicity. The average wavelength of the integrating sphere is 0.5 $\mu$m. The camera is Point Grey Corporation's FL2-20S4M-C CCD. The effective number of pixels is $1600 \times 1200$, and the size of a single pixel is 4.4 $\mu$m $\times$ 4.4 $\mu$m. A CCD camera with a relatively small pixel size is selected to catch more image details. The CCD camera is located on a 6D adjusting mount. The expected defocus is realized by moving the CCD camera back and forth along the direction of the incident chief ray, and a micrometer is used to monitor the defocus amount, as shown in Fig. 6. The initial position of the CCD camera is determined in the aligning process, in which the actual defocus $W_{020}$ of the optical system is practically zero. This initial position can also be regarded as the nominal ideal image plane.

As our first step, we image a star point of 20 $\mu$m diameter; its image could be regarded as the PSF. In total, 11 PSF images are collected, as shown in Fig. 7. The size of the star point should be 8.8 $\mu$m based on the focal length of the collimator and the size of the CCD pixel. However, we didn't have a star point of the right size at that time, so we used a 20 $\mu$m diameter star point instead. The range of defocus of these 11 images is from $-1.25\lambda$ to $1.25\lambda$, and the increment between two adjacent images is $0.25\lambda$. The actual movement range of the CCD camera $\Delta D$ is about 800 $\mu$m ($-400-400$ $\mu$m) based on the primary optics that $\Delta D$ equals $8(F/\#)^2 \cdot W_{020}$. One can see, as shown in Fig. 7, that all the PSF images are nearly the same despite different defocus, and they show the expected triangular distribution of the ideal PSF.

We proposed a simple method to evaluate the similarity of these PSF images. The length of the tail of the PSF in both the $x$ direction and the $y$ direction is selected to be the performance parameter, as shown in Fig. 8. Digital image processing operations are used to measure the lengths, which are shown in Table 2. One end of the tail is the centroid of the central spot, and the other end is close to the terminal of the tail. One can see that the shape and the size of these PSF images are similar. Also, the length in the
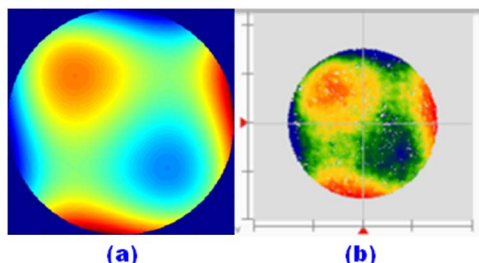


Fig. 4. (Color online) (a) Ideal wavefront map of the wavefront coded system, (b) Actual wavefront map of the wavefront coded system obtained with the Phasecam 5030 interferometer of 4D Corp.

**Table 1. Coefficients of the 7th, 8th, 10th, and 11th Zernike Polynomials of the Measured Wavefront**

| Term of Zernike Polynomial | Value |
|---|---|
| 7th | 0.4331 |
| 8th | 0.4426 |
| 10th | 0.4504 |
| 11th | −0.4455 |
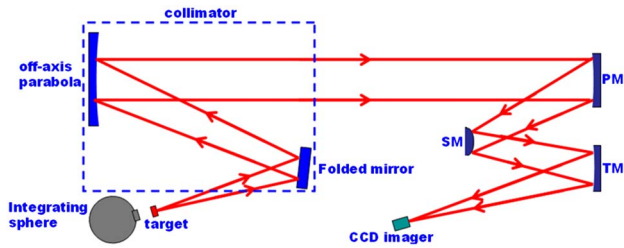
Fig. 5. (Color online) Sketch of the experiment setup.



Fig. 7. (Color online) PSF image of the system with defocus aberration from $-1.25\lambda$ to $1.25\lambda$ and the ideal PSF image (bottom right).

$x$ direction or the $y$ direction is a little smaller than the theoretical expectation. The main reason for this is that the signal at the end of the PSF tails is so weak that it is intermixed with the noise of the CCD camera and is not considered in the computation. Furthermore, only the main part of the PSF, which is actually a 13 pixel × 13 pixel area, is applied in the image restoration. It has been verified that ignoring the marginal area of the PSF has very little effect on the restored image quality.

The third plate of WT1005-62 resolution patterns is imaged as shown in Fig. 9. On the plate are 25 bar pattern groups of different spatial frequencies. The spatial frequency of the first group is $25l$ p/mm, and the spatial frequency of the 25th group is $50l$ p/mm. The spatial frequency of one group is $2^{1/2}$ times that of the former group. Because the cut-off frequency of the optical system is $57.2l$ p/mm, we are concerned with the 16th group, the spatial frequency of which is about $29.75l$ p/mm. The spatial frequency of the image of the 16th group will be doubled ($59.5l$ p/mm) because the magnifying ratio of the system is 2. In total, 11 images are recorded, as shown in Fig. 9, and the position of the image plane is the same as that of the 11 PSF images of the last experiment. For brevity, only the images of the 16th group are provided, as shown in Fig. 10. Note that the image quality is nearly invariant, despite different image plane positions, but the image quality is depressed.

It has been emphasized that one of the most important characteristics of the WFC system is that the quality of intermediate images remains almost the same in the extended DOF. The structure similarity (SSIM) is applied to evaluate the coincidence degree of the captured images with different defocus. The SSIM proposed by Wang et al. [19] is considered to be a more direct way to compare the structures between the reference image and the actual image, based on the assumption that the human visual system is highly adapted to extract structural information from the viewing field. The definition of SSIM is
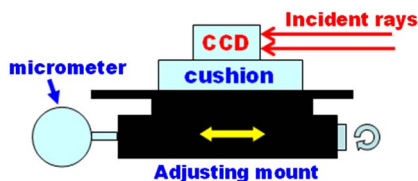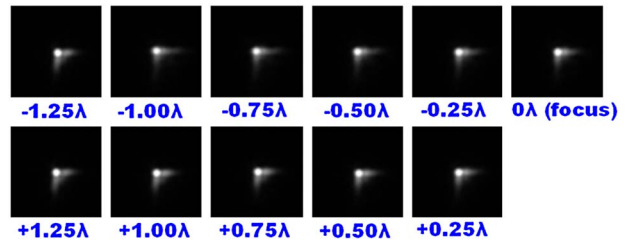
given in Eq. (5). It can be seen that the SSIM measurement comprises three relatively independent comparisons: luminance, contrast, and structure with their respective weight:

$$\text{SSIM}(x,y) = [l(x,y)]^\alpha [c(x,y)]^\beta [s(x,y)]^\gamma \quad \alpha,\beta,\gamma > 0, \quad (5)$$

where

$$l(x,y) = \frac{2\mu_r\mu_e + C_1}{\mu_r^2 + \mu_e^2 + C_1} C_1 = (K_1 L)^2 K_1 \ll 1,$$

$$c(x,y) = \frac{2\sigma_r\sigma_e + C_2}{\sigma_r^2 + \sigma_e^2 + C_2} C_2 = (K_2 L)^2 K_2 \ll 1,$$

$$s(x,y) = \frac{\sigma_{re} + C_3}{\sigma_r\sigma_e + C_3} C_3 = C_2/2,$$

$$\sigma_r = \left[\frac{1}{N-1}\sum_{i=1}^{N}(r_i - \mu_r)^2\right]^{1/2}$$

$$\sigma_e = \left[\frac{1}{N-1}\sum_{i=1}^{N}(e_i - \mu_e)^2\right]^{1/2},$$

$$\sigma_{re} = \frac{1}{N-1}\sum_{i=1}^{N}(r_i - \mu_r)(e_i - \mu_e),$$

In Eq. (3), $l(x,y)$, $c(x,y)$ and $s(x,y)$ stand for the influencing factors of luminance, contrast, and structure; $\alpha$, $\beta$, and $\gamma$ are the right coefficients of their corresponding terms; $\mu_r$ and $\mu_e$ are the average grey values of the reference image and the estimated image; $\sigma_r$ and $\sigma_e$ are the standard deviations of the reference image and the estimated image; $\sigma_{re}$ is the correlation coefficient, $L$ equals 255 for an 8 bit quantified image; $r_i$ and $e_i$ are the grey values of corresponding pixels in the reference image and the estimated image; $C_1$, $C_2$,



Fig. 6. (Color online) Sketch of the CCD camera and its adjustment in the direction of incident chief rays.
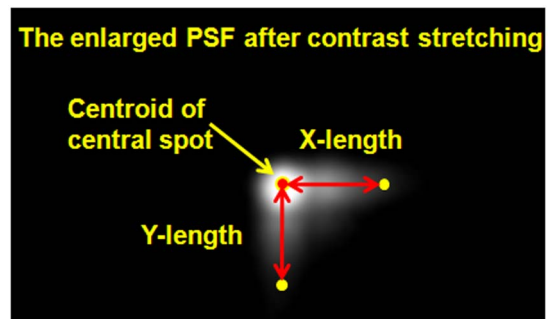


Fig. 8. (Color online) Sketch of the length of the tail of the PSF in $x$ direction and $y$ direction.

| Table 2. Length of the Tail of the 11 PSF Images in $x$ and $y$ Directions | | |
|---|---|---|
| PSF | $x$ Length (pixels) | $y$ Length (pixels) |
| −5 DOF ($W_{020} = -1.25\lambda$) | 18.0278 | 16.0312 |
| −4 DOF ($W_{020} = -1.00\lambda$) | 18.0278 | 15.0333 |
| −3 DOF ($W_{020} = -0.75\lambda$) | 17.1172 | 16.0312 |
| −2 DOF ($W_{020} = -0.50\lambda$) | 16.0312 | 15.0333 |
| −1 DOF ($W_{020} = -0.25\lambda$) | 16.0312 | 16.0312 |
| 0 DOF ($W_{020} = 0\lambda$) | 16.0312 | 16.0312 |
| 1 DOF ($W_{020} = 0.25\lambda$) | 16.0312 | 15.0333 |
| 2 DOF ($W_{020} = 0.50\lambda$) | 16.0312 | 15.0333 |
| 3 DOF ($W_{020} = 0.75\lambda$) | 17.0294 | 16.0312 |
| 4 DOF ($W_{020} = 1.00\lambda$) | 17.0294 | 17.0294 |
| 5 DOF ($W_{020} = 1.25\lambda$) | 18.0278 | 17.0294 |

| Table 3. SSIM of the Images with Different Defocus | |
|---|---|
| Image | SSIM |
| −5 DOF ($W_{020} = -1.25\lambda$) | 0.830691 |
| −4 DOF ($W_{020} = -1.00\lambda$) | 0.828082 |
| −3 DOF ($W_{020} = -0.75\lambda$) | 0.832574 |
| −2 DOF ($W_{020} = -0.50\lambda$) | 0.841528 |
| −1 DOF ($W_{020} = -0.25\lambda$) | 0.836016 |
| 0 DOF ($W_{020} = 0\lambda$) | 1 |
| 1 DOF ($W_{020} = 0.25\lambda$) | 0.83111 |
| 2 DOF ($W_{020} = 0.50\lambda$) | 0.827755 |
| 3 DOF ($W_{020} = 0.75\lambda$) | 0.828693 |
| 4 DOF ($W_{020} = 1.00\lambda$) | 0.829013 |
| 5 DOF ($W_{020} = 1.25\lambda$) | 0.821319 |

and $C_3$ are constants determined by $K_1$ and $K_2$ to avoid instability when other terms in the denominator are very close to zero; $K_1$ and $K_2$ are small empirical constant. In our calculation, $\alpha$, $\beta$, and $\gamma$ are all set to 1 as in most applications, and $K_1$ and $K_2$ are fixed as suggested in [19]. The image captured in the nominal ideal image plane is set as the reference image and the SSIM values of other images are computed according to that image, as shown in Table 3. Note that the SSIM values remain within the range 0.82–0.836, which indicates the high similarity among these images with different defocus.

## 5. Image Restoration

According to the WFC theory, the degraded images obtained by CCD directly are intermediate and need
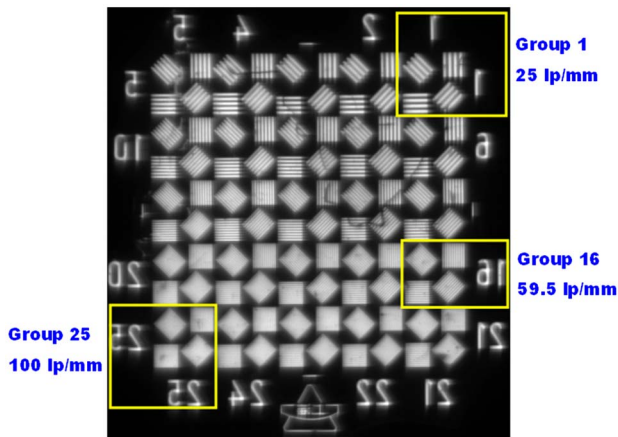


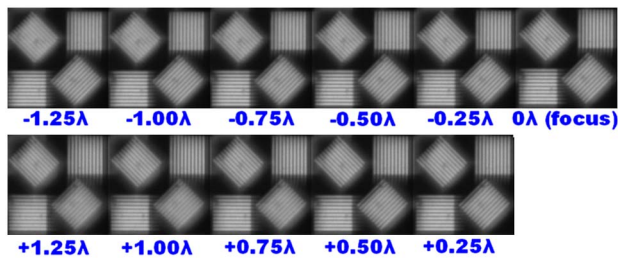Fig. 9. (Color online) Image of the third plate of WT1005-62 resolution patterns.



Fig. 10. (Color online) Original images of the 16th group resolution pattern with defocus aberration from −1.25λ to 1.25λ.
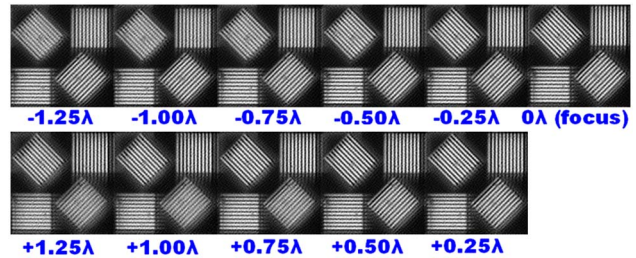
further restoration. Thus, the final step of the experiment is to restore all the images through the same Wiener filter, as shown in Fig. 11. The deconvolution core is transferred from the PSF of the nominal image plane ($W_{020} = 0$) and applied to the restoration of each image. Note that both the definition and the contrast of the restored images are improved. However, the improvement is not as good as expected. This is mainly because the PSF is not obtained by imaging the star point at the theoretical size and needs to be resampled before being applied in the filter. Therefore, some useful information about the PSF, especially in the high frequency domain, may be lost or scrambled, which limits the precision of the restoration.

Because there is no reference image, the no-reference (NR) image quality assessment is applied. The root mean square error (RMSE), the Laplacian sum (LS), and the information entropy (IE) are selected to estimate the quality of captured images and restored images as shown in Table 4 [20,21]. The definition of RMSE, LS, and LE are shown in Eq. (6):

$$\text{RMSE} = \left( \frac{1}{MN} \sum_{i=1}^{M} \sum_{j=1}^{N} (f_{i,j} - f_{\text{mean}})^2 \right)^{1/2}$$

$$\text{LS} = \frac{\sum_{i=2}^{M-1} \sum_{j=2}^{N-1} (8f_{i,j} - \sum_{a=i-1}^{a=i+1} \sum_{b=j-1}^{b=j+1} f_{a,b})}{(M-2)(N-2)}$$

$$\text{when } a = i \ b = j, \quad f_{a,b} = 0$$

$$\text{IE} = -\sum_{i=1}^{L} p(g_i) \log_2 p(g_i) (\text{unit} : \text{bit/pix}) \quad (6)$$

where $M$ and $N$ are the dimensions of the estimated image, $f_{i,j}$ is the grey value of the pixel in the $i$th row



Fig. 11. (Color online) Restored images of the 16th group resolution pattern with defocus aberration from −1.25λ to 1.25λ.

**Table 4. Comparison of RMSE and PSNR Among Captured Images and Restored Images**

| | Captured Images | | | Restored Images | | |
|---|---|---|---|---|---|---|
| | RMSE | LS | IE (bit/pix) | RMSE | LS | LE (bit/pix) |
| $-5$ DOF ($W_{020} = -1.25\lambda$) | 59.4018 | 40.1303 | 7.3305 | 67.6405 | 237.1427 | 7.6553 |
| $-4$ DOF ($W_{020} = -1.00\lambda$) | 59.9102 | 41.3435 | 7.3335 | 68.2870 | 237.8265 | 7.6471 |
| $-3$ DOF ($W_{020} = -0.75\lambda$) | 60.0807 | 42.2221 | 7.3478 | 68.4736 | 241.8276 | 7.6365 |
| $-2$ DOF ($W_{020} = -0.50\lambda$) | 60.5241 | 45.9697 | 7.3554 | 69.4036 | 256.9291 | 7.5986 |
| $-1$ DOF ($W_{020} = -0.25\lambda$) | 60.6640 | 48.0314 | 7.3640 | 69.7394 | 266.6394 | 7.5479 |
| 0 DOF ($W_{020} = 0\lambda$) | 60.5947 | 49.1598 | 7.3729 | 69.7638 | 273.8225 | 7.5078 |
| 1 DOF ($W_{020} = 0.25\lambda$) | 60.4343 | 48.1554 | 7.3766 | 69.6138 | 270.7295 | 7.5506 |
| 2 DOF ($W_{020} = 0.50\lambda$) | 60.4296 | 48.2262 | 7.3823 | 69.9292 | 270.3071 | 7.5214 |
| 3 DOF ($W_{020} = 0.75\lambda$) | 59.9213 | 44.5288 | 7.3705 | 69.0155 | 254.0007 | 7.5771 |
| 4 DOF ($W_{020} = 1.00\lambda$) | 59.5533 | 43.2008 | 7.3715 | 68.4975 | 248.1492 | 7.6042 |
| 5 DOF ($W_{020} = 1.25\lambda$) | 58.9370 | 40.7566 | 7.3593 | 67.4312 | 242.4944 | 7.6303 |

and $j$th line, $f_{\mathrm{mean}}$ is the average grey value of the whole estimated image, $f_{a,b}$ stands for the eight pixels around $f_{i,j}$, $L$ is the grey level (256 for an 8 bit image), $p(g_i)$ is the probability of the grey value $g_i$ ($g_i = 0 - 255$ for an 8 bit image), which can be obtained through the histogram.

Notice that the RMSE applied here is just a metric of contrast of a single image, which is different from the RMSE referred to full-reference image quality assessment. The larger the RMSE is, the clearer the image. The LS can be regarded as a metric of sharpness of contour. The larger the LS is, the sharper the contour of the edges. The IE is a statistical measure of randomness that can be used to characterize the texture of the image. The larger the IE is, the more information that one pixel contains and the clearer the image is in this situation. It can be observed from Fig. 10 and Table 4 that the quality of the restored image is enhanced in definition and contrast: the RMSE of all the restored images improves to greater than 67.4, the LS increases to greater than 237, and the LE increases to greater than 7.5.

## 6. Conclusion

The alignment, an imaging experiment, and restoration of an off-axis TMA system with WFC technology are described in this paper. It can be proven through the experiment that the application of WFC technology can extend the DOF of a TMA system, and the intermediate image can be restored with the measured PSF. The quality of the restored image can be further improved if a more precise PSF is provided. A more efficient algorithm of intermediate image restoration, acquisition of a more precise PSF, and more accurate assembly of the WFC system are planned for future work.

## References

1. E. R. Dowski and W. T. Cathey, "Extended depth of field through wave-front coding," Appl. Opt. **34**, 1859–1866 (1995).
2. S. Bradbum, W. T. Cathey, and E. R. Dowski, "Realizations of focus invariance in optical-digital systems with wave-front coding," Appl. Opt. **36**, 9157–9166 (1997).
3. R. Narayanswamy, A. E. Baron, V. Chumachenko, and A. Greengard, "Applications of wavefront coded imaging," Proc. SPIE **5299**, 163–174 (2004).
4. E. R. Dowski, R. H. Cormack, and S. D. Saramab, "Wavefront coding: jointly optimized optical and digital imaging systems," Proc. SPIE **4041**, 114–120 (2000).
5. K. Kubala, E. R. Dowski, J. Kobus, and B. Brown, "Design and optimization of aberration and error invariant space telescope systems," Proc. SPIE **5524**, 54–65 (2004).
6. R. Porras, S. Vázquez, and J. Castro, "Wavefront coding technology in the optical design of astronomical instruments," Proc. SPIE **5622**, 796–800 (2004).
7. S. Mezouari and A. R. Harvey, "Wavefront coding for aberration compensation in thermal imaging systems," Proc. SPIE **4442**, 34–42 (2001).
8. W. Chi and N. George, "Smart camera with extended depth of field," Proc. SPIE **6024**, 602424 (2005).
9. R. Narayanswamy, P. E. X. Silveira, H. Setty, V. P. Pauca, and J. Gracht, "Extended depth-of-field iris recognition system for a workstation environment," Proc. SPIE **5779**, 41–50 (2005).
10. G. A. Cirino and L. G. Neto, "Design of cubic-phase distribution lenses for passive infrared motion sensors," Proc. SPIE **5073**, 476–484 (2003).
11. E. J. Tremblay, J. Rutkowski, and I. Tamayo, "Relaxing the alignment and fabrication tolerances of thin annular folded imaging systems using wavefront coding," Appl. Opt. **46**, 6751–6758 (2007).
12. P. Mouroulis, "Depth of field extension with spherical optics," Opt. Express **16**, 12995–13004 (2008).
13. S. H. Lee, N. C. Park, and Y. P. Park, "Breaking diffraction limit of a small $f$-number compact camera using wavefront coding," Opt. Express **16**, 13569–13578 (2008).
14. W. B. Wetherell and D. A. Womble, "All-reflective three element objective," U.S. patent 4,240,707 (23 December 1980).
15. F. Yan and X. J. Zhang, "A design of off-axis three mirror anastigmatic optical system with wavefront coding technology," Opt. Eng. **47**, 063001 (2008).
16. F. Yan and X. J. Zhang, "Optimization of an off-axis three-mirror anastigmatic system with wavefront coding technology based on MTF invariance," Opt. Express **17**, 16809–16819 (2009).
17. F. Yan, L. G. Zheng, and X. J. Zhang, "Image restoration of an off-axis three mirror anastigmatic optical system with wavefront coding technology," Opt. Eng. **47**, 017006 (2008).

18. F. Yan, D. Fan, B. Z. Zhang, L. H. Yin, R. G. Li, and X. J. Zhang, "Manufacturing and testing of a cubic SiC surface," Chin. Opt. Lett. **7**, 534–536 (2009).
19. Z. Wang, A. C. Bovik, H. R. Sheikh, and E. P. Simoncelli, "Image quality assessment: from error visibility to structural similarity," IEEE Trans. Image Process. **13**, 600–612 (2004).
20. B. R. Frieden, "Maximum-information data processing: application to optical signals," J. Opt. Soc. Am. **71**, 294–303 (1981).
21. D. Kermisch, "A deterministic analysis of the maximum entropy image restoration method and of some related methods," J. Opt. Soc. Am. **67**, 1154–1159 (1977).